Modeling compositional changes in binary solid solutions under ion bombardment: Application to the Ar^+ bombardment of MgAl alloys

F. Reichel,[1,2] L. P. H. Jeurgens,[1,*] and E. J. Mittemeijer[1,2]
[1]*Max Planck Institute for Metals Research, Heisenbergstraße 3, D-70569 Stuttgart, Germany*
[2]*Institute for Physical Metallurgy, University of Stuttgart, Heisenbergstraße 3, D-70569 Stuttgart, Germany*
(Received 20 July 2005; revised manuscript received 17 October 2005; published 11 January 2006)

A model is presented which describes the steady state composition-depth profile developing in the surface adjacent region of a binary solid solution under continuous ion bombardment as a function of the bulk alloying content and the type and kinetic energy of the incident ions. To this end, the combined processes of preferential sputtering and bombardment-enhanced Gibbsian segregation are considered, while accounting for the depth and concentration dependence of the vacancy-enhanced diffusion coefficient in the solid. The model was applied to Ar^+ bombardment of Mg-based MgAl alloys for various bulk Al contents (2.63–7.31 at. %) and various incident Ar^+ ion energies (0.1–3 keV). Very good agreement was obtained between the calculated, steady state Al concentration-depth profiles and the "as-measured" ones as determined experimentally by Auger electron spectroscopy, angle-resolved x-ray photoelectron spectroscopy, and ion scattering spectroscopy.

DOI: 10.1103/PhysRevB.73.024103 PACS number(s): 79.20.Ap, 79.20.Rf, 68.35.Dv, 64.75.+g

I. INTRODUCTION

Upon bombardment of the surface of a solid with incident ions, several processes are initiated at the outer surface and in the subsurface region. The incident ions may be either reflected from the surface (ion scattering), or deposited on the surface (ion sputter deposition), or buried within the subsurface region (ion implantation). Upon collision of high-energy incident ions (with a kinetic energy of, say, >500 eV) with the solid, a cascade of events will be initiated involving the ejection of electron(s) and atom(s) from the surface region, and the formation of nonequilibrium point defects (i.e., vacancies and interstitials) in the subsurface region in combination with a perturbation of the initial arrangement of the atoms in the solid. For the ion-bombardment of multicomponent targets, a distinction is made between primary and secondary processes.[1] The primary processes are concerned with the preferential sputtering behavior of a target with a given composition, whereas the secondary processes deal with further changes of the target composition due to effects initiated by the ion bombardment.

The preferential ejection of one species from the target surface is a primary process, further designated as preferential sputtering (PS), and results in compositional changes that are confined to the outer surface. PS is governed by the relative masses and the relative surface binding energies of the alloy constituents, with the lighter and/or weaker bonded atoms being sputtered away preferentially (see Refs. 1 and 2).

Displacement mixing, ion implantation, vacancy-enhanced diffusion, and bombardment-induced segregation are secondary processes and induce compositional changes over a depth range extending far beyond the topmost surface layers. Displacement mixing (DM) comprises recoil implantation and cascade mixing. Recoil implantation is a direct result of the knockon event between the incident ion and the target atoms and depends on the ion and target masses due to preferential momentum transfer (predominantly along the beam direction; see Refs. 3 and 4). Cascade mixing is a random-walk process resulting from the movement of higher-order recoil atoms and is the dominant atom-transport mechanism at temperatures (T) below $\sim 0.2T^m$ (T^m is the alloy's melting temperature), where point defects are immobile. At temperatures above $\sim 0.2T^m$, thermally activated diffusion becomes the dominant atom-transport mechanism. In the temperature range of $\sim 0.2T^m < T < \sim 0.6T^m$, the concentration of bombardment-induced point defects exceeds the concentration of equilibrium point defects by orders of magnitude, thereby strongly promoting thermally activated diffusion (see Refs. 3 and 5). This process, which drives the system towards compositional equilibrium, is further designated here as vacancy-enhanced diffusion (VED).[6] Bombardment-induced defects can migrate before being eliminated by mutual recombination or annihilation at extended sinks (i.e., the surface, dislocations, or grain boundaries). Because these defect fluxes are always associated with fluxes of atoms, any preferential association of defects with a particular alloy constituent (as a consequence of a significant difference in the enthalpy of vacancy migration between the alloy constituents) will couple a net flux of this constituent to the defect fluxes. This preferential defect-solute flux coupling tends to move the alloy away from compositional equilibrium, a process designated as bombardment-induced segregation (BIS) (also referred to as radiation-induced segregation; see Refs. 3 and 7).

Concurrently with the aforementioned primary and secondary ion-bombardment processes, the preferential segregation of one alloy constituent to the free surface may occur in order for the system to reduce its surface free energy. In the absence of nonequilibrium point defects in the alloy, this process is referred to as Gibbsian segregation. However, for the alloy under continuous ion bombardment, Gibbsian segregation is strongly promoted by DM and, in particular, by VED for temperatures above $\sim 0.2T^m$ (see above). This process is designated here as bombardment-enhanced Gibbsian segregation (BEGS) (see Refs. 3 and 8).

Thus, for the ion bombardment of a multiple-component solid, compositional, structural, and electronic changes are

induced both at the surface and in the subsurface region, thereby affecting the physical and chemical properties of the solid (see Refs. 9–14. Consequently, understanding and controlling ion bombardment of solid surfaces is of great interest for a broad range of application areas, such as surface coatings, steel industry, integrated optics and microelectronics (e.g., magnetic and optical devices, thin film resistors, solid electrolytes, lasers, wear-resistant coatings, surface etching or polishing). For example, by well-defined ion bombardment treatments of solid surfaces, the thermal and electrical conductivity, hardness, wear, friction, adhesion, density, morphology, or corrosion resistance may be improved (see Refs. 9–14).

Nevertheless, up to date, fundamental and comprehensive knowledge leading to a satisfactory, quantitative description of the different processes governing the micro-structural changes in alloys under continuous ion bombardment lacks. Only, a few attempts have been made to model the compositional changes in the subsurface region of alloys under ion bombardment.[3,8,15,16] In most of these studies the depth and concentration dependence of the vacancy-enhanced chemical diffusion coefficient is not considered. Also, the effect of the incident ion energy is generally unaccounted for. Consequently, these model predictions showed significant discrepancies with corresponding experimental observations (see Refs. 17 and 18), which were conducted for binary alloys such as CuAu,[19–24] CuZr,[18] NiZr,[17] and CuNi.[25,26]

In the present contribution, a novel model is presented, which describes the steady state concentration-depth and vacancy-depth profiles developing in the subsurface region of a binary solid solution under continuous ion bombardment as a function of the nominal alloy composition, and the type and energy of the incident ions in the temperature range of $\sim 0.2T^m < T < \sim 0.6T^m$. In the model, the combined processes of PS and BEGS are considered, while accounting for the depth and concentration dependence of the vacancy-enhanced diffusion coefficient in the alloy.

The model is applied to the bombardment of Mg-based MgAl solid solutions at room temperature (i.e., $\sim 0.3T^m$) with Ar^+ ions of kinetic energies in the range of 0.1–3 keV and for various Al alloying contents in the range of 2.63–7.31 at. %. The calculated steady state composition-depth profiles are compared with the corresponding measured Al concentrations in the bombarded alloy, as determined experimentally using Auger electron spectroscopy (AES), angle-resolved (AR) x-ray photoelectron spectroscopy (XPS) and ion scattering Spectroscopy (ISS). Although Mg-based MgAl alloys are important materials for application as light-weight alloys (see Refs. 27 and 28), only very limited knowledge exists on the ion bombardment of Mg-based MgAl alloys (see Ref. 29).

II. THEORY

Ion bombardment of a binary alloy causes material removal from the surface (sputtering). Hence, volume diffusion within the surface adjacent region of the ion-bombarded binary alloy can be described by Fick's second law modified for the occurrence of a moving boundary, representing the inward migrating surface (see Refs. 15 and 30), i.e.,

$$\frac{\partial C_i(z)}{\partial t} = \frac{\partial}{\partial z}\left[\tilde{D}(z)\frac{\partial C_i(z)}{\partial z}\right] + v\left[\frac{\partial C_i(z)}{\partial z}\right] \quad (i = A,B), \quad (1)$$

where $C_i(z)$ is the concentration of the ith component at depth z beneath the migrating surface (at position $z=0$) at time t, $\tilde{D}(z)$ is the depth-dependent chemical diffusion (or interdiffusion) coefficient, and v denotes the sputtering velocity (i.e., the velocity of the inwardly moving surface per unit time), which is calculated from

$$v = \frac{JY_{AB}M_{AB}}{\rho_{AB}N_{\mathrm{Av}}}, \quad (2)$$

where J is the total ion flux (i.e., the sputter current density), Y_{AB} denotes the total sputter yield (the average number of atoms leaving the alloy surface per incident ion), M_{AB} and ρ_{AB} are the molar mass and the density of the alloy, and N_{Av} is Avogadro's constant.

For the continuous ion bombardment of a homogeneous binary alloy, a steady-state composition-depth profile will be setup in the alloy as soon as the composition of the sputtered-atom flux equals the bulk composition of the alloy (as dictated by the law of conservation of matter). The occurrence of a steady state implies that

$$\frac{\partial C_i(z)}{\partial t} = 0 \quad (i = A,B). \quad (3)$$

Then also that the total sputter yield and thereby the sputtering velocity [see Eq. (2)] are constants.

For the ion bombardment of substitutional binary solid solutions in the temperature range of $\sim 0.2T^m < T < \sim 0.6T^m$, the secondary processes of displacement mixing (DM) (comprising recoil implantation and cascade mixing, see Sec. I) and bombardment-induced segregation (BIS) can generally be neglected (see Sec. I and Refs. 4, 5, and 7). (i) Recoil implantation is only important in binary systems with relatively large mass differences (as is seldom the case in solid solutions). (ii) The relative contribution to atom-transport by cascade mixing only predominates for $T < \sim 0.2T^m$. (iii) BIS is only significant for relatively large differences in enthalpy of point defect migration of the alloying constituents (as is generally not the case for solid solutions). Therefore, in the following theoretical treatment on the ion bombardment of substitutional binary solid solutions in the temperature range of $\sim 0.2T^m < T < \sim 0.6T^m$, only the competing processes of preferential sputtering (PS) and bombardment-enhanced Gibbsian segregation (BEGS) are considered, while accounting for the depth and concentration dependence of the vacancy-enhanced diffusion coefficient in the alloy (see Sec. I).

The process of BEGS results in a continuous exchange of atoms between the outermost surface layer and the alloy subsurface region. If the atom exchange is sufficiently fast, the concentrations of the alloying constituents at the surface C_i^0 will approach their thermal equilibrium values (as determined by pure Gibbsian segregation), i.e.,

$$\frac{C_A^0}{C_B^0} = \frac{C_A^\infty}{C_B^\infty} \exp\left(\frac{Q}{RT}\right), \tag{4a}$$

where $C_i^\infty = C_i(z \to \infty)$ denotes the bulk concentration of the ith alloy constituent at depth $z \to \infty$ below the alloy surface, R is the gas constant, T the temperature, and Q is the segregation enthalpy. A rough estimate of the segregation enthalpy Q in Eq. (4a) is obtained from the sublimation enthalpies $\Delta H_i^s (>0)$ of the respective pure elements according to

$$Q = \frac{\Delta H_B^s - \Delta H_A^s}{4}. \tag{4b}$$

For most alloys the difference in sublimation enthalpy between elements A and B is sufficiently large to approach an equilibrium atom fraction of the non-segregating element at the surface of zero [see Eqs. (4a) and (4b)].

To a first approximation, sputtering implies removal of atoms from only the outermost surface.[8] Consequently, under the constraint of a steady state a continuous transport of the segregating element from the second atom layer to the inwardly moving surface (i.e., a continuous depletion of the segregating element from the second atom layer) occurs during sputtering. Then the atom fraction of the non-segregating element in the second atom layer approaches the value of one, provided that the rate of supply of the segregating element from the interior of the alloy to the depleted second layer is relatively slow. Sputtering is the much faster process as compared to BEGS.[31] In the model it thus can be assumed that the composition of the actual first atom layer is determined by PS [see Eq. (5b) below]. The composition of the second atom layer is dictated by BEGS according to Eqs. (1)–(3), i.e., under the constraint of an inwardly moving surface. To solve Eqs. (1)–(3) for the atom layers two and deeper, as a boundary condition the atom fraction of the non-segregating element (taken here as $i=A$) is taken equal to one in a hypothetical "first atom layer." The second boundary condition for solving the Eqs. (1)–(3) follows from the requirement of zero flux at $z \to \infty$ [i.e., $C_{i=A}(z \to \infty) = C_A^\infty$]. This leads to a steady state concentration profile for the nonsegregating element A according to

$$C_A(z > 0) = C_A^\infty + (1 - C_A^\infty) \exp\left[- v \int_0^z \frac{dz'}{\tilde{D}(z')} \right], \tag{5a}$$

where $C_A^\infty = C_A(z \to \infty)$ denotes the bulk concentration of the nonsegregation element A at depth $z \to \infty$ below the alloy surface (with the concentration in atom fraction). This solution is only applied for depths equal to and larger than the depth of the second atom layer.

The true composition at the ion-bombarded surface (i.e., $z=0$, the first atom layer) is taken equal to the composition as dictated by the preferential sputtering (see Refs. 8 and 32):

$$C_A(z=0) = \left(\frac{C_B^\infty y_A}{C_A^\infty y_B} + 1 \right)^{-1}, \tag{5b}$$

where y_i is the component sputter yield of the ith alloy constituent, defined as the average number of atoms of element i per unit concentration of i atoms leaving the alloy surface per incident ion [$Y_{AB} = y_A c_A + y_B c_B$; for Y_{AB} see Eq. (2)]. The value for the relative sputter yield, i.e., y_A / y_B in Eq. (5b), is governed by the relative masses (i.e., atomic numbers) and the relative surface binding energies of the elements in the alloy, with the lighter and/or weaker bonded atoms being sputtered away preferentially; the value of the relative sputter yield is generally independent of the type, flux and energy of the incident ions (see Refs. 2 and 8).

The depth-dependent chemical diffusion coefficient in Eq. (5a) is given by (see Ref. 33)

$$\tilde{D}(z) = [C_B(z) D_A^*(z) + C_A(z) D_B^*(z)] \left\{ 1 + \frac{\partial \ln \gamma_i}{\partial \ln C_i} \right\} \ (i = A,B), \tag{6a}$$

where $D_i^*(z)$ is the self-diffusion coefficient of the element i and γ_i is the activity coefficient of the element i in the solid solution. The vacancy mechanism is the dominant diffusion mechanism in pure metals and substitutional binary solid solutions. Then, in the present case, the self-diffusion coefficient $D_i^*(z)$ is dependent on the depth z, as it depends on the depth-dependent vacancy concentration $C_v(z)$. For the continuous bombardment of substitutional solid solutions with high-energy ions (i.e., of, say, kinetic energy >0.1 keV), the formation of vacancies within the alloy subsurface region is solely determined by the cascade processes within the alloy as induced by the collisions. If the vacancy concentration-depth profile is known, the corresponding self-diffusion coefficient $D_i^*(z)$ in Eq. (6a) can be taken as (see Ref. 33)

$$D_i^*(z) = K C_v(z) \exp\left(\frac{\Delta S_i^m}{R}\right) \exp\left(-\frac{\Delta H_i^m}{RT}\right) \ (i = A,B), \tag{6b}$$

where ΔS_i^m and ΔH_i^m are the entropy and enthalpy of atom (vacancy) migration in the pure metal i, respectively (K can be taken as a constant, the value of which depends on the frequency of atom vibration and incorporates a geometrical factor).[33]

As verified by Monte Carlo simulations of the effect of impact of high-energy ions at a localized position on a binary alloy surface (as performed in the present study using the SRIM program[34]), the induced cascade processes typically produce a peak maximum in the vacancy concentration-depth profile centered at certain depth below the free surface. Because vacancies created at small depths become easily annihilated at the free surface, the peak maximum is positioned directly below, but not at, the outer surface. In these Monte Carlo simulations defect migration by thermal diffusion (and also BEGS, VED and an inward migrating surface) are not considered. However, for the ion-bombarded alloy in steady state at $\sim 0.2 T^m < T < \sim 0.6 T^m$, the produced defects can flow either towards the free surface or from the peak damage region towards regions of lower defect density in the interior of the alloy. The resulting steady-state vacancy concentration profile can then be described by a spike at a certain depth below the surface with exponential decaying tails towards the free surface and the interior of the alloy. A flexible description of such a vacancy concentration-depth profile as a

function of both the alloy composition and the flux and kinetic energy of the bombarding ions is given by

$$C_v(z) = C_v^{\mathrm{eq}} + \alpha\left[1 - \exp\left(-\frac{z}{\beta}\right)\right]^{\chi} \exp\left(-\frac{z}{\beta}\right), \qquad (7)$$

where C_v^{eq} is the thermal equilibrium vacancy concentration within the alloy at temperature T, and the parameters α, β, and χ define the vacancy concentration profile and depend on the flux and kinetic energy of the bombarding ions and the alloy composition. The parameters β and χ determine the depth of the spike in the vacancy concentration-depth profile and the rate of the exponential decay of the vacancy concentration towards the interior of the alloy, respectively. The parameter α controls the height of the spike in (and thereby the total area under) the vacancy concentration-depth profile. The exact position and height of the spike in the vacancy concentration-depth profile, as well as the rate of exponential decay of the vacancy concentration towards the interior of the alloy, depend on the type, flux and energy of the incident ions and on the composition of the alloy under study (see Sec. V).

III. EXPERIMENTAL

A. Specimen preparation

Disc-shaped, polycrystalline MgAl alloys (ϕ=10 mm; thickness=1 mm) with a nominal Al content of 2.63, 5.78, and 7.31 at. % (purity >99.998 at. %) were prepared (and their surfaces ground and polished down to 0.25 μm) as described in detail in Ref. 28. The average grain size of the weakly textured specimen (as determined using x-ray diffractometry) is in the range of 50–100 μm. Also two corresponding element standards of pure Mg and Al (as required for the composition analysis by surface analytical techniques; see Sec. IV A) were prepared according to the above procedure.

B. Specimen treatment and analysis

All ion bombardment treatments and corresponding AES, AR-XPS, or ISS measurements were performed in ultrahigh vacuum (UHV) chambers (base pressure $<3\times10^{-8}$ Pa) operating at room temperature. For each alloy surface under study (as well as for the Mg and Al standards; see Sec. III A), first any surface contamination was removed by sputter cleaning with Ar^+ ions of the same kinetic energy as used for the subsequent ion bombardment treatment (see below), until no other elements than Mg and Al were detected (by using either AES, AR-XPS, or ISS; see below). The area for sputter cleaning was always taken at least three times larger than the analysis area used for the subsequent ion bombardment investigation (see below). The alloy substrates as obtained after sputter cleaning will be further designated as bare substrates.

Next, an ion bombardment treatment of the bare alloy surfaces was employed by alternating steps of ion bombardment for 1 min with Ar^+ ions of constant kinetic energy in the range of 0.1–3 keV and subsequent analysis (i.e., as started 1 s after the ion bombardment treatment). Each ion bombardment step was performed with a focussed Ar^+ beam rastering the alloy surface (raster: 400×400 μm^2, 5000×5000 μm^2, and 3000×3000 μm^2 for AES, AR-XPS, and ISS, respectively; current densities as reported in Table I; angle of incidence of 41°–45° between the ion beam and the specimen surface normal). The alternating steps of ion bombardment and analysis were performed until no visible changes in the recorded Al and Mg signal intensities occur between the successive steps, i.e., until a steady state composition-depth profile has been set up within the alloy subsurface region. Steady state concentrations in the alloy subsurface region were generally achieved after only a few steps of ion bombardment (the precise time depending on the incident ion energy and the alloy composition). For each alloy composition (2.63–7.31 at. % Al) and incident ion energy (0.1–3 keV), the alternating steps of ion bombardment and subsequent analysis were continued for about 10–30 min after reaching steady state signal intensities (to increase the accuracy in the subsequent determination of the corresponding steady state composition). As determined by the AES analysis (see below), the measured steady state concentrations remained constant for about 20 min after switching off the ion beam (after which the alloy surface gets contaminated with oxygen and/or carbon). It was also found (by AES) that the measured steady state concentrations were independent of the crystallographic orientation of the investigated grains, the incident ion flux, the applied sequence of incident ion energies, and the surface roughness (which increased upon bombardment of high-energetic Ar^+ ions, >1 keV).

AES measurements were performed using a JEOL JAMP-7830F equipped with a field emission electron gun and a hemi-spherical analyzer. Spectra of the *KLL* and *LVV* Auger lines of Mg and Al, as well as the C *KLL* and O *KLL* lines (for contamination control) were recorded by scanning a specimen surface area of 10×10 μm^2 with a primary electron beam of 10 keV and 12 nA (detection angle of θ=25° with respect to the surface normal).

AR-XPS analysis was performed with a Thermo VG Thetaprobe 500 system employing monochromatic incident Al $K\alpha$ radiation ($h\nu$=1486.68 eV; spot size 400 μm). AR-XPS spectra of the Mg 2p, Al 2p, and O 1s binding-energy regions (step size 0.1 eV; constant pass energy 100 eV) were recorded in the so-called parallel data acquisition mode[35] by detecting the photoelectrons simultaneously over the angular range of $(\theta,\psi)=(23°,43°)$ to $(\theta,\psi)=(83°,94°)$ in eight ranges of 7.5° each (for details, see Ref. 35). Here, the interdependent angles θ and ψ are defined between the direction of the detected photoelectrons and the sample surface normal and between the direction of the detected photoelectrons and the incident photon beam, respectively. The AR-XPS spectra were measured at nine defined locations on the specimen surface (spot size 400 μm), respectively, equally distributed over an analysis area of 3×3 mm^2 and the thus measured nine spectra for each binding-energy region averaged for each angular range of photoelectron detection.

ISS analysis was also performed with the Thermo VG Thetaprobe 500 system by switching lens voltages of the hemispherical analyser and employing a focussed 1 keV He^+ incident ion beam (current ~50 nA). As for the AR-XPS

TABLE I. Values for the physical and chemical constants used in the numerical computations [see Eqs. (2) and (5)–(7)]. The Al content is given as subscript in at. %.

Symbol	Constituent, alloy composition or ion energy	Value	Unit	Source
D_i^0	i=Mg	1.77	10^{-4}m^2 s^{-1}	Ref. 39
	i=Al	0.1		Ref. 40
ΔH_i^{v}	i=Mg	0.8	eV	Refs. 44 and 45
	i=Al	0.67		Refs. 46–48
ΔS_i^{v}	i=Mg	3.42	10^{-23} J K^{-1}	Ref. 46
	i=Al	0.97		Ref. 48
ΔH_i^{m}	i=Mg	0.5	eV	Refs. 45 and 49
	i=Al	0.61		Ref. 47
$\left\{1+\frac{\partial \ln \gamma_{\mathrm{Al}}}{\partial \ln C_{\mathrm{Al}}}\right\}$	$MgAl_{2.63}$	0.6250		Ref. 41
	$MgAl_{5.78}$	0.5377		
	$MgAl_{7.31}$	0.4311		
$y_{\mathrm{Mg}}/y_{\mathrm{Al}}$		3.95		ISS, present study
ρ	$MgAl_{2.63}$	1.756	10^3 kg m^{-3}	XRD, present study
	$MgAl_{5.78}$	1.780		
	$MgAl_{7.31}$	1.787		
J_{AES}	E_{Ar^+}=0.1 keV	0.63	10^{18} m^{-2} s^{-1}	present study
	E_{Ar^+}=0.2 keV	1.25		
	E_{Ar^+}=0.5 keV	18.7		
	E_{Ar^+}=1.0 keV	62.4		
	E_{Ar^+}=2.0 keV	74.9		
	E_{Ar^+}=3.0 keV	87.4		
$J_{\mathrm{XPS,ISS}}$	E_{Ar^+}=1.0 keV	0.94	10^{18} m^{-2} s^{-1}	present study
	E_{Ar^+}=2.0 keV	1.02		
	E_{Ar^+}=3.0 keV	1.77		
$\mathrm{Y}_{\mathrm{MgAl}}$	for various C_{Al}^{∞} and E_{Ar^+}	0.63–4.71		from SRIM (Ref. 34)

spectra, the ISS spectra (step size 1 eV; constant pass energy 200 eV) were recorded in the parallel data acquisition mode by detecting the photoelectrons simultaneously over the angular range of $(\theta,\psi)=(23°,43°)$ to $(\theta,\psi)=(83°,94°)$ in eight ranges of 7.5° each (for details, see Ref. 35).

IV. EVALUATION OF COMPOSITION-DEPTH PROFILES

A. Composition data from AES, AR-XPS, and ISS

The "as-measured" concentration of element i, $\langle C_i^{\mathrm{exp}}\rangle$, can be determined from the intensities I_i of elements in the alloy, as resolved from the measured AES, AR-XPS, or ISS spectra, according to[36]

$$\langle C_i^{\mathrm{exp}}\rangle = \frac{I_i S_i}{\sum_{n=A,B} I_n S_n}, \tag{8a}$$

where S_i is the element-, signal-, and technique-specific sensitivity factor, which is obtained for a binary alloy, AB, from the respective pure element standard intensity I_i^{∞} for AES, XPS, and ISS, using the formulas

$$S_i^{\mathrm{AES}} = \frac{[1+r_i^{\infty}(E_{i_X},E_0,\varphi)]\lambda^{\mathrm{eff},\infty}(E_{i_{XYZ}})\rho^{\infty}}{I_i^{\infty}[1+r_i^{AB}(E_{i_X},E_0,\varphi)]\lambda^{\mathrm{eff},AB}(E_{i_{XYZ}})\rho^{AB}}, \tag{8b}$$

$$S_i^{\mathrm{XPS}} = \frac{\lambda^{\mathrm{eff},\infty}(E_{i_X})\rho^{\infty}}{I_i^{\infty}\lambda^{\mathrm{eff},AB}(E_{i_X})\rho^{AB}}, \tag{8c}$$

and

$$S_i^{\mathrm{ISS}} = \frac{\rho^{\infty}}{I_i^{\infty}\rho^{AB}}, \tag{8d}$$

respectively. The superscripts AB and ∞ in Eqs. (8b)–(8d) denote the alloy and the pure element standard, respectively; $r_i(E_{i_X},E_0,\varphi)$ is the backscatter correction factor accounting for the additional ionization of the core level X with binding energy E_{i_X}, arising from backscattered electrons in the solid for primary incident electrons of energy E_0 under an angle of incidence φ with respect to the surface normal; $\lambda^{\mathrm{eff}}(E)$ is the effective attenuation length (EAL) of the detected XYZ Au-

TABLE II. Calculated values for the EAL's λ^{eff} (in nm), and the backscatter correction factors r, as required in the AES quantification (see Secs. III B and IV A).

Symbol	Line	pure Mg	$MgAl_{2.63}$	$MgAl_{5.78}$	$MgAl_{7.31}$	pure Al
$\lambda^{\text{eff}}_{\text{Mg}}$	LVV	0.386	0.386	0.385	0.384	
	KLL	3.218	3.199	3.176	3.167	
$\lambda^{\text{eff}}_{\text{Al}}$	LVV		0.442	0.440	0.439	0.416
	KLL		3.654	3.627	3.617	3.025
r_{Mg}	LVV	0.6746	0.675	0.676	0.676	
	KLL	0.4372	0.438	0.438	0.439	
r_{Al}	LVV		0.660	0.661	0.661	0.683
	KLL		0.416	0.416	0.417	0.432

ger electrons or photoelectrons of the core level X with kinetic energy $E_{i_{XYZ}}$ or E_{i_X}, respectively; ρ is the total atomic volume density in the solid for AES and XPS and the total atomic surface density at the solid surface for ISS. The values for the various EALs λ^{eff} and the backscattering correction factors $r_i(E_{i_X}, E_0, \varphi)$, as required for the AES and AR-XPS quantifications, have been given in Tables II and III (as calculated according to the procedure described in Refs. 36 and 37).

In the quantitative AES analysis, the peak-to-peak heights in the seven-point differentiated spectra were used as a measure for I_i (see Ref. 36). In the AR-XPS quantification, the total metallic Mg $2p$ and Al $2p$ primary zero-loss intensities, as resolved from the measured spectra of the alloy according to the procedure described in detail in Ref. 35, were employed as measure for I_i. In the ISS quantification, the integrated areas of the Mg and Al main peaks were employed as measure for I_{Al} and I_{Mg}. These integrated intensities were resolved from the measured ISS spectra by linear-least squares fitting, while employing the corresponding peak shapes and positions of the respective main peaks as obtained from the pure element spectra. In the ISS quantification, it is assumed that the neutralization behavior is the same for the pure element standards and the concerned alloys, in accordance with Ref. 38.

Because of the exponential decay of the XPS and AES signal intensity with increasing depth of origin for the photoelectron or Auger electron, respectively, the measured values of $\langle C_i^{\text{exp}} \rangle$ for the XPS and AES analysis [see Eq. (8a)] represent attenuation-length weighted, averaged values over the probed depth range in the subsurface region. The depth (as measured perpendicular to the sample surface) for which the signal intensity has dropped to $1/e$ (36.8%) of its value for origin of the signal at the surface equals $d = \lambda^{\text{eff}} \cos\theta$, with θ as the angle between the direction of the detected electrons and the surface normal.[36] For the ISS analysis, the measured value of $\langle C_i^{\text{exp}} \rangle$ represents the concentration of element i at the outer surface (first atom layer).

B. Composition data from model fitting

For the binary MgAl alloys investigated, Mg is both the lighter and weaker-bonded alloy constituent,[32] and is therefore sputtered preferentially and also simultaneously segregating to the ion-bombarded alloy surface (i.e., element A in Sec. II corresponds in this work with Al).

The theoretical, steady state Al concentration-depth profiles (i.e., the Al alloying concentration $C_{\text{Al}}(z)$ as a function of the depth z below the alloy surface) for the various alloy compositions and incident ion energies considered were calculated using Eqs. (5)–(7), after choosing the fit parameters (i.e., α, β, and χ; see below) and adopting appropriate values for the other parameters, as given in Table I. The integral in Eq. (5a) was calculated by numerical integration using the trapezoidal rule. No values for the entropy of atom migration are available to calculate the self diffusion coefficients $D^*_{\text{Mg}}(z)$ and $D^*_{\text{Al}}(z)$ using Eq. (6b) in Sec. II. Only values for the respective preexponential (Arrhenius) constants D^0_{Mg} and D^0_{Al} of the self-diffusion coefficients have been reported in the literature.[39,40] Therefore, Eq. (6b) is transformed into

$$D_i^*(z) = D_i^0 \exp\left(\frac{\Delta S_i^v}{R}\right)^{-1} C_v(z) \exp\left(-\frac{\Delta H_i^m}{RT}\right) \quad (i = \text{Mg, Al}), \tag{9}$$

where ΔS_i^v is the entropy of vacancy formation of theelement i. The thermodynamic factor $\{1 + \partial \ln \gamma_{\text{Al}} / \partial \ln C_{\text{Al}}\}$ in Eq. (6a) was obtained applying the THERMO-CALC software and employing the COST507 database.[41]

To compare the calculated concentration-depth profiles (i.e., C_{Al} as a function of z) with the corresponding averaged experimental concentration values $\langle C^{\text{exp}}_{\text{Al}} \rangle$ as determined from AES and AR-XPS, averaged calculated concentration values $\langle C^{\text{calc}}_{\text{Al}} \rangle$ (corresponding to the measured values $\langle C^{\text{exp}}_{\text{Al}} \rangle$) were obtained using (see Ref. 36)

$$\langle C^{\text{calc}}_{\text{Al}} \rangle = \frac{\int_0^\infty C^{\text{calc}}_{\text{Al}}(z) \exp\left(-\frac{z}{\lambda^{\text{eff,MgAl}}(E_{\text{Al}_{XYZ}}) \cos\theta}\right) dz}{\int_0^\infty C^{\text{calc}}_{\text{Al}}(z) \exp\left(-\frac{z}{\lambda^{\text{eff,MgAl}}_{\text{Al}} \cos\theta}\right) dz + \frac{\lambda^{\text{eff,alloy}}_{\text{Al}}}{\lambda^{\text{eff,alloy}}_{\text{Mg}}} \int_0^\infty C^{\text{calc}}_{\text{Mg}}(z) \exp\left(-\frac{z}{\lambda^{\text{eff,MgAl}}_{\text{Mg}} \cos\theta}\right) dz}, \tag{10}$$

TABLE III. Calculated values for the EAL's (in nm), as required in the AR-XPS quantification (see Sec. III B). The interdependent detection angles θ and ψ are defined as the angles between the direction of the detected photoelectrons and the sample surface normal and between the direction of the detected photoelectrons and the incident photons, respectively (see Secs. III A and III B and Ref. 35).

(θ,ψ) (deg.)	Symbol	pure Mg	$MgAl_{2.63}$	$MgAl_{5.78}$	$MgAl_{7.31}$	pure Al
(26.8,45.9)	λ_{Mg}^{eff}	3.795	3.772	3.745	3.735	
	λ_{Al}^{eff}		3.724	3.697	3.687	3.090
(34.3,51.7)	λ_{Mg}^{eff}	3.770	3.748	3.720	3.710	
	λ_{Al}^{eff}		3.697	3.670	3.660	3.062
(41.8,57.8)	λ_{Mg}^{eff}	3.748	3.725	3.698	3.688	
	λ_{Al}^{eff}		3.673	3.646	3.636	3.037
(49.3,64.2)	λ_{Mg}^{eff}	3.728	3.705	3.678	3.668	
	λ_{Al}^{eff}		3.652	3.625	3.615	3.016
(56.8,70.6)	λ_{Mg}^{eff}	3.710	3.688	3.660	3.650	
	λ_{Al}^{eff}		3.634	3.607	3.597	2.997
(64.3,77.2)	λ_{Mg}^{eff}	3.695	3.672	3.645	3.635	
	λ_{Al}^{eff}		3.618	3.591	3.581	2.980
(71.8,83.8)	λ_{Mg}^{eff}	3.680	3.657	3.630	3.620	
	λ_{Al}^{eff}		3.603	3.576	3.567	2.965
(79.3,90.4)	λ_{Mg}^{eff}	3.664	3.641	3.614	3.604	
	λ_{Al}^{eff}		3.587	3.560	3.551	2.948

where $\lambda_{Al}^{eff,MgAl}$ and $\lambda_{Mg}^{eff,MgAl}$ are the effective attenuation lengths (EAL) of the concerned Auger or photoelectrons originating from Al and Mg atoms in the alloy, respectively, and traveling with a given kinetic energy through the alloy (see Sec. III A). The measured Al concentrations as determined with ISS can be directly compared with the calculated Al concentration in the first atom layer of the bombarded alloy surface [see Eq. (5b), as determined only by preferential sputtering].

Fitting of the calculated concentration-depth profiles to the experimental data (as obtained using AR-XPS, AES, and ISS, see Sec. V) was performed by minimizing the sum of squared differences between the set of calculated and experimental "as-measured" Al concentration values (i.e., $\langle C_{Al}^{calc}\rangle$ and $\langle C_{Al}^{exp}\rangle$, respectively), while varying only the parameters α, β, and χ (using the Nelder-Mead simplex method as implemented in Matlab, see Ref. 42). In the fitting, all experimental concentration values, as obtained from the various techniques for various alloying contents and various sputter ion energies, were fitted simultaneously. Thus the fit parameters α, β, and χ, which define the height and shape of the vacancy concentration-depth profile (see Sec. II), are the only unknowns in the fit procedure. Note that, because the parameter α, which determines the (total) vacancy concentration (see Sec. II), and the chemical diffusion coefficient $\tilde{D}$ are interdependent coefficients [compare Eqs. (6a), (6b), (7), and (9)], small errors in the input values of D_i^0, ΔS_i^v, ΔH_i^m and/or $\{1+\partial \ln \gamma_{Al}/\partial \ln C_{Al}\}$ will be compensated by a change in the value of α determined by the fittings without affecting the calculated Al concentration-depth profiles.

On the basis of the outcome of a systematic parameter study on the dependence of the fit parameters α, β, and χ on the alloy composition (C_{Al}^{∞}) and the incident ion energy (E_{Ar^+}), the fit parameter α (determining the area under the vacancy-concentration profile, see Sec. II) was shown to depend on both C_{Al}^{∞} and E_{Ar^+}. The fit parameter β (mainly determining the position of the spike in the vacancy-concentration profile, see Sec. II) depends only on E_{Ar^+}, whereas the fit parameter χ (mainly determining the exponential decay of the vacancy concentration towards the interior of the alloy, see Sec. II) was shown to be dependent on only C_{Al}^{∞}. The values for α and β, as resulting from the fitting, have been plotted as a function E_{Ar^+}, for various Al bulk concentrations, in Figs. 1(a) and 1(b), respectively. The values for χ, which are independent of E_{Ar^+}, have been plotted as a function of C_{Al}^{∞} in Fig. 1(c).

V. RESULTS: EXPERIMENT VERSUS MODEL

Experimental and fitted concentration values have been indicated by the solid and open markers in Fig. 2, respectively. Clearly, for all alloy compositions and incident ion energies (E_{Ar^+}) studied, very good agreement exists between the calculated and experimental "as-measured" alloying concentrations (also note that the "as-measured" concentrations as determined independently by AES and AR-XPS agree well, see Figs. 2(b), 2(d), and 2(f)). "As-measured" steady state concentrations values, as determined by AR-XPS (E_{Ar^+}=3 keV for $MgAl_{2.63}$, $MgAl_{5.78}$, and $MgAl_{7.31}$) and ISS (E_{Ar^+}=2 and 3 keV for $MgAl_{5.78}$) were also fitted, but are not shown here. The thus obtained, corresponding, calculated Al and vacancy concentration-depth profiles have been presented in Figs. 3 and 4 for the ion-bombarded $MgAl_{2.63}$ and $MgAl_{7.31}$ alloy, respectively.

Due to PS of Mg in combination with simultaneous BEGS of Mg to the surface, an overall enrichment of Al in

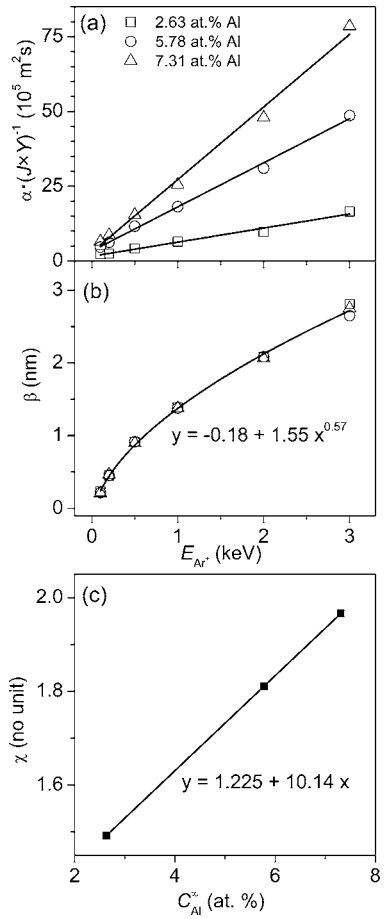

FIG. 1. Optimized values for (a) the fit parameter α and (b) the fit parameter β both as a function of the incident Ar^+ ion energy E_{Ar^+} and (c) the fit parameter χ as a function of the Al bulk concentration C_{Al}^{∞} each for continuous Ar^+ bombardment of MgAl alloys of various compositions.

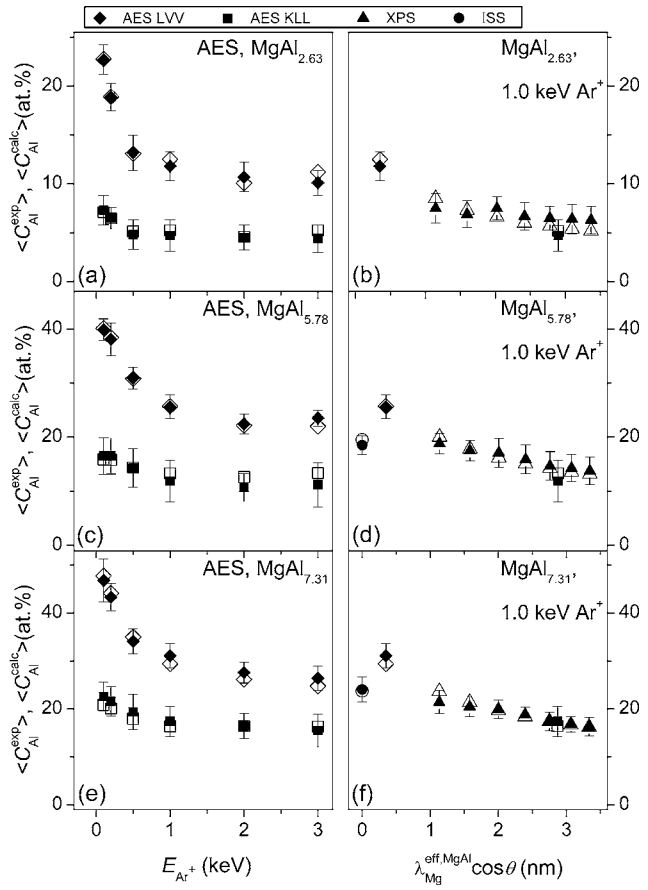

FIG. 2. Experimental $\langle C_{Al}^{exp} \rangle$ (solid markers) and calculated $\langle C_{Al}^{cal} \rangle$ (open markers) Al concentrations as a function of the incident ion energy E_{Ar^+} (AES) and the escape depth $\lambda_{Mg}^{eff,MgAl} \cos\theta$ (for the different techniques, with ISS pertaining to zero escape depth, see Sec. IV A) as determined for the steady state of Ar^+ bombardment of MgAl alloys with an Al content of 2.63 at. % [(a) and (b)], 5.78 at. % [(c) and (d)], and 7.31 at. % [(e) and (f)]. The experimental Al concentrations, as determined using AES for the KLL and LVV peaks, are plotted as a function of E_{Ar^+} for the respective alloy compositions in (a), (c), and (e). The "as-measured" Al concentrations, as determined using AES, AR-XPS, and ISS, are presented as a function of the escape depth for $E_{Ar^+}=1$ keV for the respective alloy compositions in (b), (d), and (f).

the alloy subsurface region is probed using AES, AR-XPS, and ISS (see Fig. 2). However, a distinct drop occurs in the degree of Al enrichment at the outer surface (i.e., the first atom layer), as observed with ISS [see Figs. 2(b), 2(d), and 2(f)]. Yet, the concentration of Al at the very surface (as measured with ISS) is larger than its bulk concentration, which is a direct consequence of PS of Mg. These Al concentration depth profiles reflect the competition of the concurrent processes of BEGS of Mg and PS of Mg. The observations are consistent with the model presented in Sec. II.

The degree of "as-measured" Al enrichment in the alloy subsurface region decreases with both increasing E_{Ar^+} and increasing depth below the alloy surface. This agrees with the, calculated, "true" Al concentration-depth profiles (Fig. 3). The bombarded alloy reaches its bulk composition at a depth value below the sample surface, which increases with increasing E_{Ar^+} and also, too a much lesser extent, with increasing C_{Al}^{∞} (in the range 2 to 12 nm; Fig. 3). The steady state, "as-measured," depth-averaged Al concentrations in the probed subsurface region can be as high as 46 at. % Al for $E_{Ar^+}=0.1$ keV and $MgAl_{7.31}$ [Fig. 2(e)], corresponding to a "real" Al concentration in the second atom layer of about 70 at. % (Fig. 3).

The calculated, steady state vacancy concentration-depth profiles (also) depend strongly on the incident Ar^+ ion energy (Fig. 4). Both the concentration and depth range of bombardment-enhanced vacancies in the alloy subsurface region increase with increasing E_{Ar^+}. Defining z_v^{max} as the depth at which the vacancy concentration has fallen to a value below 5% of its maximum concentration value, it follows that the value of z_v^{max} increases roughly linearly with increasing E_{Ar^+} (see Fig. 5). The value of z_v^{max} obtained here as the outcome of the Al concentration-depth profile fitting, is in very good agreement with the corresponding depth in the nonsteady-state (see Sec. II) vacancy concentration-depth profile as obtained from Monte Carlo simulations using the SRIM software[34] (see Fig. 5).

As follows from comparison of Figs. 3 and 4, a direct relationship exists between the steady state Al and vacancy

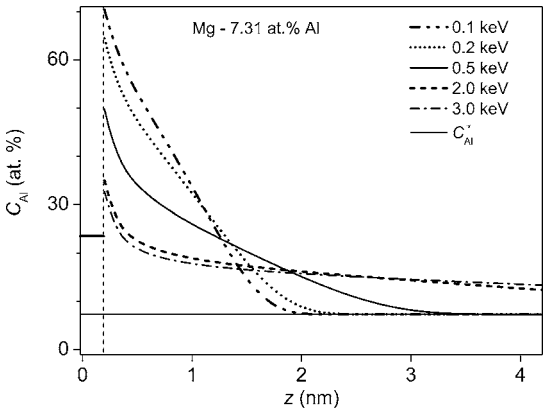

FIG. 3. Calculated steady state Al concentration-depth profile for the Mg 7.31 at. % Al alloy under continuous Ar^+ bombardment for various incident ion energies E_{Ar^+}. Note that the composition of the first atom layer at the alloy surface is independent of E_{Ar^+}, since it is only determined by the preferential sputtering [see Eq. (5b), Sec. II].

concentration-depth profiles. If the process of VED could be neglected, the Al enrichment in the second atom layer beneath the surface would be independent on E_{Ar^+}, because the heat of segregation is independent of E_{Ar^+} [see Eq. (4b)]. In reality, the Al enrichment in the alloy subsurface region due to concurrent PS of Mg and BEGS of Mg is reduced for higher E_{Ar^+} (i.e., the Al concentration profiles become flattened, Fig. 3), because of the increased depth range and increased residual vacancy concentration with increasing E_{Ar^+} (i.e., VED is promoted with increasing E_{Ar^+}).

As indicated by results obtained for the fitted value of α with increasing C_{Al}^{∞} [Fig. 1(a)], the steady state vacancy concentration in the alloy subsurface region not only increases with the incident Ar^+ energy, but also increases with the bulk Al concentration. This implies that the vacancies in the MgAl alloys are stabilized by the presence of Al.

It follows, as an outcome of the concentration-depth profile fitting, that the parameter α is proportional to the product of the ion flux J and the sputter yield Y_{MgAl} [see Fig. 1(a)]. Consequently, the interdependent values of the vacancy concentration and the chemical diffusion coefficient are also proportional to the product $J \times Y_{MgAl}$ [see Eqs. (6b) and (7) and neglecting the equilibrium, thermal vacancy concentration]. A proportionality between the (vacancy-enhanced) chemical diffusion coefficient and the ion flux has been reported previously.[43] On the basis of the same reasoning, the quotient in Eq. (5a) of the sputter velocity [see Eq. (2)] and the (vacancy-enhanced) chemical diffusion coefficient (both proportional with $J \times Y_{MgAl}$), and thereby the steady state Al concentration-depth profile, do *not* depend on $J \times Y_{MgAl}$, which agrees with the experimental observations in the present study (see Sec. III B).

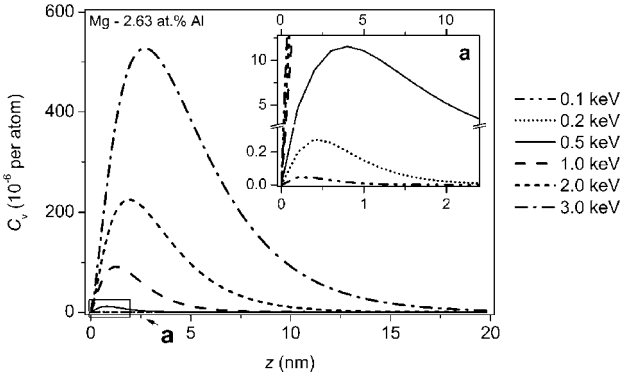

FIG. 4. Calculated steady state vacancy concentration-depth profile for the Mg 2.63 at. % Al alloy under continuous Ar^+ bombardment for various incident ion energies E_{Ar^+}.

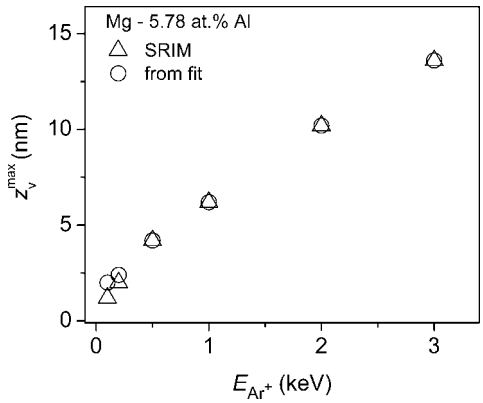

FIG. 5. The depth where the vacancy concentration has fallen to a value below 5% of its maximum concentration value z_v^{max} as determined from the vacancy concentration-depth profiles determined by fitting to the experimental concentration values (○) and as determined by Monte Carlo simulations using the SRIM software (Ref. 34) (△), both as a function of the incident Ar^+ ion energy E_{Ar^+} for the Mg 5.78 at. % Al alloy.

VI. CONCLUSIONS

The steady state concentration-depth profiles of the alloying element and of the (bombardment-generated) vacancies in a binary solid solution under continuous ion bombardment within the temperature range $\sim 0.2T^m < T < \sim 0.6T^m$ can be well described by the combined processes of preferential sputtering and bombardment enhanced Gibbsian segregation, provided that the depth and concentration dependence of the vacancy-enhanced diffusion coefficient in the alloy is accounted for.

The model was applied to Mg-based MgAl alloys under Ar^+ bombardment for various bulk Al alloying contents and incident Ar^+ energies at room temperature. Good agreement between the calculated steady state composition-depth profiles in the ion-bombarded alloy and the corresponding, measured concentration values (as determined by AES, AR-XPS, and ISS) was obtained for various incident ion energies and bulk alloy concentrations by employing only three fit parameters: the parameters α, β, and γ, which determine the shape of the vacancy concentration-depth profile in the alloy subsurface. The calculated steady state composition-depth profiles in the alloy do not depend on the product of the incident ion flux and the sputter yield, in accordance with the experimental observations.

Due to preferential sputtering of Mg in combination with the simultaneous bombardment-enhanced Gibbsian segregation of Mg to the free surface, a strong Al-enrichment develops in the alloy subsurface region. The degree of Al enrichment in the alloy subsurface region *decreases* with increasing incident Ar^+ energy, with increasing depth below the alloy surface and with increasing Al bulk content. The bombarded alloy reaches its bulk composition at a depth below the sample surface in the range of 2 to 12 nm (for E_{Ar^+} in the range of 0.1 to 3 keV and C_{Al}^{∞} in the range of 2.63–7.31 at. %). A distinct drop in the degree of Al enrichment occurs at the outer surface, with a composition governed by preferential sputtering.

The concentration and depth range of the bombardment-enhanced vacancies in the alloy subsurface region *increase* with increasing incident Ar^+ energy and with increasing Al bulk content, because the vacancies are stabilized by the presence of Al. Consequently, vacancy-enhanced diffusion in the subsurface region increases with increasing incident Ar^+ energy and with increasing Al bulk content, resulting in a flattening of the Al concentration-depth profiles.

ACKNOWLEDGMENTS

The authors are indebted to Dr. C. Linsmeier and Dr. E. Taglauer of the Max-Planck-Institut für Plasmaphysik, Garching bei München, for additional ISS analysis and to Dipl.-Ing. B. Siegle for the AES analysis.

*Email address: l.p.h.jeurgens@mf.mpg.de.

[1] P. Sigmund, A. Oliva, and G. Falcone, Nucl. Instrum. Methods Phys. Res. **194**, 541 (1982).
[2] G. Betz, Surf. Sci. **92**, 283 (1980).
[3] N. Q. Lam and H. Wiedersich, Nucl. Instrum. Methods Phys. Res. B **18**, 471 (1987).
[4] P. Sigmund, Nucl. Instrum. Methods Phys. Res. B **34**, 15 (1988).
[5] H. Wiedersich, Nucl. Instrum. Methods Phys. Res. B **7-8**, 1 (1985).
[6] The vacancy mechanism is the dominant diffusion mechanism in substitutional binary solid solutions, as considered in the present work. Therefore, the term vacancy-enhanced diffusion (instead of "radiation-enhanced diffusion," see Refs. 3 and 5) is used here.
[7] H. Wiedersich, P. R. Okamoto, and N. Q. Lam, J. Nucl. Mater. **83**, 98 (1979).
[8] R. Kelly, Surf. Interface Anal. **7**, 1 (1985).
[9] P. D. Townsend, J. C. Kelly, and N. E. W. Hartley, *Ion Implantation, Sputtering and their Applications* (Academic Press, London, 1976), p. 247.
[10] L. J. Johnson, in *Ion Bombardment Modification of Surfaces*, edited by O. Auciello and R. Kelly (Elsevier, Amsterdam, 1984), Chap. 9, p. 361.
[11] O. Auciello, in *Ion Bombardment Modification of Surfaces*, edited by O. Auciello and R. Kelly (Elsevier, Amsterdam, 1984), Chap. 11, p. 435.
[12] J. A. Thornton, in *Deposition Technologies for Films and Coatings*, edited by R. F. Bunshah (Noyes Publications, Park Ridge, New Jersey, 1982), Chap. 5, p. 170.
[13] D. M. Mattox, in *Deposition Technologies for Films and Coatings*, edited by R. F. Bunshah (Noyes Publications, Park Ridge, New Jersey, 1982), Chap. 6, p. 244.
[14] B. Chapman, *Glow Discharge Processes, Sputtering and Plasma Etching* (Wiley, New York, 1980), Chap. 6, p. 177.
[15] P. S. Ho, Surf. Sci. **72**, 253 (1978).
[16] D. G. Swartzfager, S. B. Ziemecki, and M. J. Kelley, J. Vac. Sci. Technol. **19**, 185 (1981).
[17] H. J. Kang, R. H. Roberts, S. He, D.J. O'Connor, and R. J. MacDonald, Surf. Sci. **302**, 363 (1994).
[18] H. J. Kang, C. H. Kim, N. S. Park, D. J. O'Connor, and R. J. MacDonald, Appl. Surf. Sci. **100/101**, 329 (1996).
[19] H. J. Kang, R. Shimizu, and T. Okutani, Surf. Sci. **116**, L173 (1982).
[20] H. J. Kang, E. Kawatoh, and R. Shimizu, Surf. Sci. **144**, 541 (1984).
[21] R.-S. Li, L.-X. Tu, and Y.-Z. Sun, Surf. Sci. **163**, 67 (1985).
[22] R.-S. Li, L.-X. Tu, and Y.-Z. Sun, Appl. Surf. Sci. **26**, 77 (1986).
[23] H. J. Kang, J. H. Kim, Y. S. Kim, D. W. Moon, and R. Shimizu, Surf. Sci. **226**, 93 (1990).
[24] S.-Y. Li and R.-S. Li, Surf. Interface Anal. **27**, 957 (1999).
[25] T. Okutani, M. Shikata, and R. Shimizu, Surf. Sci. **99**, L410 (1980).
[26] W. D. Roos, G. N. van Wyk, and J. du Plessis, Surf. Interface Anal. **20**, 95 (1993).
[27] G. L. Makar and J. Kruger, J. Electrochem. Soc. **137**, 414 (1990).
[28] L. P. H. Jeurgens, M. S. Vinodh, and E. J. Mittemeijer, Appl. Surf. Sci. (to be published).
[29] P. Braun, M. Arias, H. Störi, and F. P. Viehböck, Surf. Sci. **126**, 714 (1983).
[30] J. Crank, *The Mathematics of Diffusion*, 1st ed. (Clarendon Press, Oxford, 1956).
[31] The cascade effects, induced by the incident ion hitting the alloy surface, ends after about 0.1–1 ps, whereas bombardment-enhanced segregation can take many seconds to reach completion (see Ref. 8).
[32] G. Betz and G. K. Wehner, in *Topics in Applied Physics, Sputtering by Particle Bombardment I*, edited by R. Behrisch (Springer, Berlin, 1983), Vol. 52, p. 11.
[33] P. Shewmon, *Diffusion in Solids*, 2nd ed. (The Minerals, Metals & Materials Society, Warrendale, 1989), p. 66.
[34] J. F. Ziegler and J. P. Biersack, SRIM-2000.40, IBM Co., 2000.
[35] M. S. Vinodh and L. P. H. Jeurgens, Surf. Interface Anal. **36**, 1629 (2004).
[36] M. P. Seah, in *Surface Analysis by Auger and X-Ray Photoelectron Spectroscopy*, edited by D. Briggs and J. T. Grant (IM Publications and SurfaceSpectra Limited, Manchester, 2003), p. 345.
[37] A. Jablonski and C. J. Powell, Surf. Sci. Rep. **47**, 33 (2002).
[38] J.-P. Jacobs, S. Reijne, R. J. M. Elfrink, S. N. Mikhailov, H. H. Brongersma, and M. Wuttig, J. Vac. Sci. Technol. A **12**, 2308 (1994).
[39] J. Combronde and G. Brebec, Acta Metall. **19**, 1393 (1971).
[40] S. Dais, R. Messer, and A. Seeger, Mater. Sci. Forum **15-18**, 419

(1987).
[41] THERMO-CALC version M, *COST507 Light alloys database*, v2.1, 1998/2003, Thermo-Calc Software, Stockholm.
[42] MATLAB version 6.1.0.450, Release 12.1, The MathWorks, Inc., Natick, 2001.
[43] N. Itoh and K. Morita, Radiat. Eff. **80**, 163 (1984).
[44] P. Tzanetakis, J. Hillairet, and G. Revel, Phys. Status Solidi B **75**, 433 (1976).
[45] C. Mairy, J. Hillairet, and D. Schumacher, Acta Metall. **15**, 1258 (1967).
[46] R. W. Balluffi, J. Nucl. Mater. **69/70**, 240 (1978).
[47] R. W. Siegel, J. Nucl. Mater. **69/70**, 117 (1978).
[48] H.-E. Schaefer, R. Gugelmeier, M. Schmolz, and A. Seeger, Mater. Sci. Forum **15-18**, 111 (1987).
[49] J. Delaplace, J. Hillairet, J. C. Nicoud, and D. Schumacher, Phys. Status Solidi **30**, 119 (1968).